

Effects of vortex-induced velocity on the wake of a synthetic jet issuing into a turbulent boundary layer

Tim Berk, Guillaume Gomit, Bharathram Ganapathisubramani[†]

Engineering and the Environment
University of Southampton
Southampton, SO17 1BJ, UK

[†] G.Bharath@southampton.ac.uk

ABSTRACT

A synthetic jet issued in a cross flow creates a momentum deficit in the cross flow downstream of the jet. In the literature, this deficit is ascribed to viscous blockage by the jet and the up wash of low-momentum fluid caused by the vortical structures of the jet. This paper proposes and quantifies a third effect contributing to the momentum deficit: a velocity induced by the vortical structures in the direction opposite to the cross flow. A reconstruction technique – quantifying the vortex-induced velocity – is developed to determine the momentum deficit caused by the proposed effect. This is applied to a test case of a rectangular synthetic jet ($AR = 13$, $St = 0.5$, $r = 0.88$) issuing into a turbulent boundary layer ($Re_\tau = 1220$, $U_\infty = 10$ m/s, $\delta = 45$ mm). The shape of the created vortical structures is reconstructed using a combination of planar- (two-dimensional two-component) PIV in the streamwise-wall-normal plane and stereo- (two-dimensional three-component) PIV in the spanwise-wall-normal plane. The reconstructed shape consists of overlapping clockwise- and counterclockwise hairpins. With this (constant) shape known, the distribution of hairpins can be determined using the spanwise-vorticity field only. From this distribution of vortical structures the induced velocity is calculated using Biot-Savart's law. Qualitatively the induced velocity components are very similar to the equivalent measured velocity components. The streamwise momentum flux deficit per unit width at the centerline is calculated for both the induced and the measured case. After some start-up behaviour the momentum deficit for both cases becomes relatively constant. In this constant regime ($x/\delta > 1$) the momentum deficit induced by the vortical structures accounts for 90% of the measured momentum deficit. It is reasoned that the other 10% is most likely to be caused by an increase in skin friction resulting from the up wash of low-momentum fluid (and consequential down wash of high-momentum fluid).

INTRODUCTION

Synthetic jets in cross flow are widely used in applications such as mixing enhancement (M'Closkey *et al.*, 2002; Sau & Mahesh, 2008), control of turbulence (Rathnasingham & Breuer, 2003) or separation control (Dandois *et al.*, 2007). The interaction of a synthetic jet with a cross flow leads to a momentum deficit in the cross flow downstream of the jet, causing an increase in drag. For most applications minimization of this momentum deficit is of importance for the efficiency of the pursued goal. In order to minimize it, the origin of the momentum deficit needs to be understood. In the literature, the momentum deficit is often referred to as blockage (see for example Lardeau & Leschziner (2011)), or as caused by vortex induced up wash of low-momentum fluid near the wall (see for example Rathnasingham & Breuer (2003)). However, these were qualitative descriptions and do not quantify the momentum deficit in any detail. This paper proposes a third origin and quantifies its momentum deficit: a velocity induced by the created vortical structures in the direction opposite to the cross flow. Further-

more, it will be reasoned that the effects of blockage and up wash on the momentum deficit are limited. The total momentum deficit will be a combination of these three (and possibly other) factors, i.e. viscous blockage of the cross flow, vortex induced up wash of low-momentum fluid and a vortex induced velocity in the direction opposite to the cross flow. The ratio of contributions of these effects will vary with downstream distance and depends on the flow parameters and the type of vortical structures created by the synthetic jet.

A synthetic jet is formed from the working fluid by alternating blowing and suction, creating a vortex ring at the jet exit each blowing cycle. The sinusoidal velocity cycle can be characterized by a frequency, f , and a velocity magnitude, \bar{u} . The velocity magnitude used here is the mean blowing velocity, calculated as $\bar{u} = \frac{1}{T} \int_0^{T/2} u(t) dt$. The relevant parameters of the interaction between the synthetic jet and the turbulent boundary layer are described by the velocity ratio and the Strouhal number, defined as

$$r = \frac{\bar{u}}{U_\infty}, \quad (1)$$

$$St = \frac{f\delta}{U_\infty}, \quad (2)$$

with U_∞ the free-stream velocity of the cross flow and δ the boundary-layer thickness.

The vortical structures created by a synthetic jet in cross flow have been mapped onto a parameter space by Sau & Mahesh (2008). For low velocity ratios the shear in the boundary layer is strong enough to fully cancel the vorticity of opposite sign on the upstream side of the vortex ring, modifying this ring to a hairpin-like structure. The vortex ring (or hairpin) has a self-induced velocity in the wall-normal direction, transporting the ring upwards while being convected downstream by the cross flow. Since the upstream side of the hairpin is (partially or fully) cancelled, the downstream side experiences a larger self-induced velocity, causing the structure to tilt into the cross flow. This results in a hairpin structure that is very similar to eddies observed in and/or modelled for turbulent boundary layers (see for example Perry & Chong (1982)). A notable difference is that the vortical structures created by the synthetic jet are of a periodical nature and reappear at the exact same spot each cycle whereas eddies in a turbulent boundary layer have a statistical distribution.

The formed vortical structure is linked to all three origins of the momentum deficit introduced above; the fluid ejected by the synthetic jet forming this structure causes viscous blockage of the cross flow, the structure induces a velocity component in the wall-normal direction causing up wash of low-momentum fluid and it induces a streamwise velocity component in the opposite direction as

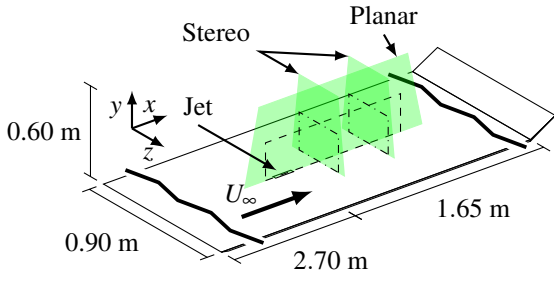


Figure 1. Schematic of experimental set-up (not to scale).

the cross flow. The present paper focusses on the velocity induced by the vortical structure in streamwise direction. This induced velocity is calculated from the vorticity field related to the velocity components relative to the incoming flow. This means the considered vorticity field is relative to the shear in the incoming boundary layer. Since the (partial) cancellation of the upstream side of the vortex ring will have cancelled an equal but opposite amount of circulation from the boundary layer, this side of the vortex ring will still be visible in this relative vorticity field. Therefore, the vortical structures presented below have a crossbar between the two legs, creating an A-shape. The velocity induced by this structure is calculated using Biot-Savart, similar to how contributions of eddies in the turbulent boundary layer are calculated (see for example recent work by de Silva *et al.* (2015) or Baidya *et al.* (2017)).

EXPERIMENTAL METHOD

Experiments are performed in the University of Southampton's 3 ft by 2 ft suction wind tunnel. The tunnel is fitted with a false floor, creating a test section of 4.35 m \times 0.60 m \times 0.90 m ($x \times y \times z$, as defined in Fig. 1). Figure 1 presents a schematic of the experimental set-up. The elliptical leading edge of the floor is fitted with a boundary-layer trip. The angle of the trailing-edge flap is adjusted to ensure a zero-pressure-gradient turbulent boundary layer at the measurement location. The turbulent boundary layer has a free-stream velocity of $U_\infty = 10$ m/s and boundary-layer thickness of $\delta = 45$ mm ($Re_\tau = 1220$). A rectangular synthetic jet (orifice dimensions $l = 13$ mm in x -direction and $d = 1$ mm in z -direction) is issued into the turbulent boundary layer, directed perpendicular to the surface. The jet is actuated at a frequency of $f = 110$ Hz and velocity of $\bar{u} = 8.8$ m/s ($St = 0.5$, $r = 0.88$). Velocity fields are measured using particle image velocimetry (PIV). Planar-PIV measurements are taken in the (x, y) -plane on the centerline of the orifice, spanning from $x = -2\delta$ to 7δ and $y = 0.05\delta$ to 2δ . For this measurement an array of three LaVision ImagerPro LX 16MP cameras is used. The planar velocity fields have a resolution of 0.34 mm per vector. Stereo-PIV measurements are taken in the (z, y) -plane at streamwise positions of 3δ and 6δ downstream of the orifice, with the plane spanning from $z = -1\delta$ to 1δ and $y = 0.05\delta$ to 2δ . For this measurement two LaVision ImagerPro LX 16MP cameras are placed at opposite sides of the test section, pointing upstream with an internal angle of 60 degrees. The stereo velocity fields have a resolution of 0.35 mm per vector. Measurements are taken phase-locked to the actuation signal at eight equidistant phases (300 image pairs per phase).

RESULTS

A combination of the planar- and stereo-PIV is used to determine the velocity induced by the vortical structures created by the synthetic jet. First, the geometry of the structure is recreated using both measurement planes. Next, the streamwise-wall-normal velocity field is used to determine the local strength (circulation) of

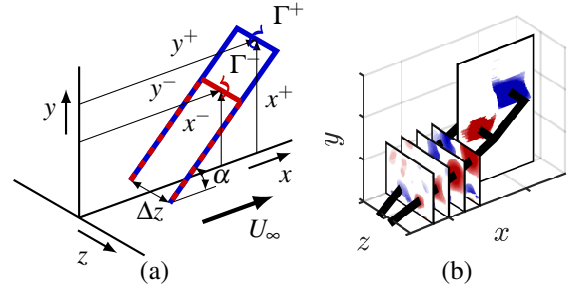


Figure 2. Geometry of modelled vortical structure (a) and visualisation of reconstruction using planar- and stereo-PIV data (b).

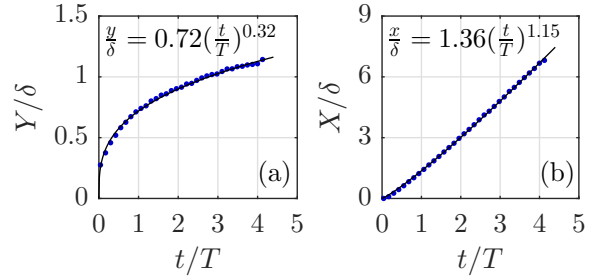


Figure 3. Evolution of the clockwise spanwise vortex in the wall-normal direction (a) and streamwise direction (b) as function of time. Data points (dots) is fitted against power laws (lines).

the structures. Both the geometry and the strength feed into a model, using Biot-Savart law to calculate the vortex-induced velocity.

Reconstruction of geometry from stereo-PIV

The geometry of the vortical structures that are created can be reconstructed using a combination of the planar- and stereo-PIV data. A schematic of the vortical structure is presented in Figure 2a. The geometry of this structure is fully described by the position of the hairpin head (x^+, y^+), the position of the crossbar (x^-, y^-), the inclination angle (α) and the separation between the legs (Δz). The circulation of the different sections is given by Γ^+ (blue line), Γ^- (red line) and $\Gamma^+ + \Gamma^-$ (red-blue dashed lines). These parameters are measured using the planar- ($x^-, y^-, \Gamma^-, x^+, y^+, \Gamma^+$) and stereo-PIV ($\alpha, \Delta z$) data. A visualisation of how the geometry is reconstructed from the data is presented in Figure 2b where spanwise and streamwise vorticity are plotted.

The four streamwise-vorticity fields presented in Figure 2b are actually measured at different phases at a single streamwise position. The streamwise velocity of the structure is used to translate the phase difference to a separation in streamwise direction. The position of the clockwise vortex is tracked in the (x, y) -plane. The wall-normal and streamwise positions of this vortex as function of time are presented in Figure 3. The evolution in both directions is fitted using a power law of the form $x/\delta = A(t/T)^n$ as indicated by the black lines. The derivative of this relation indicates a fit for the streamwise velocity and therewith the streamwise distance related to the phase difference between subsequent vorticity fields.

The streamwise-vorticity fields are presented in more detail in Figure 4, measured at $x/\delta = 3$ (top row) and $x/\delta = 6$ (bottom row). The vorticity is normalized by the mean vorticity created by the jet, given by $\omega_0 = \Gamma/(\bar{u}l/f)$. At both streamwise positions the legs of the structure are only visible during four out of eight phases. For

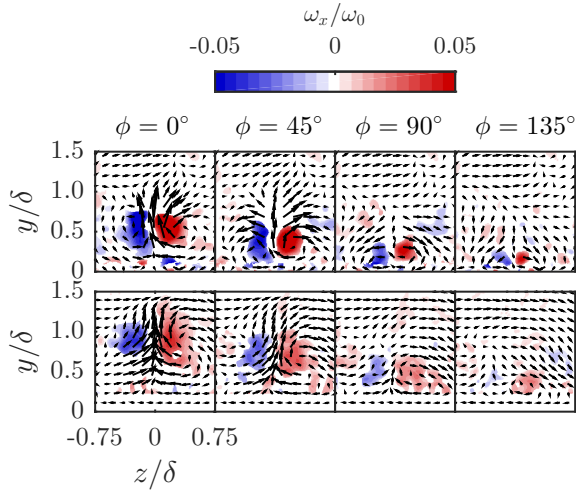


Figure 4. Streamwise vorticity measured using stereo-PIV, showing the legs of the vortical structure. The vorticity fields represent four phases (half a cycle) at $x/\delta = 3$ (top) and $x/\delta = 6$ (bottom).

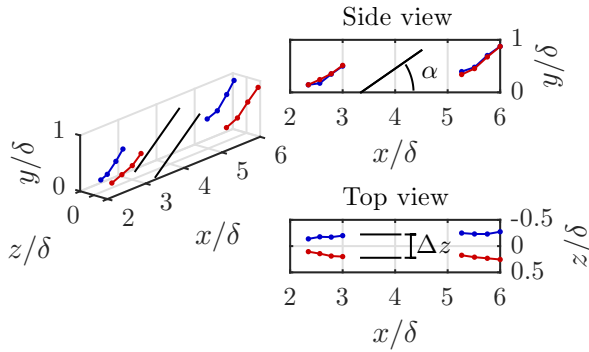


Figure 5. Measured geometry of the legs of the vortical structure at $x/\delta = 3$ and 6. Colours indicate sign of streamwise vorticity (red positive). The black structure indicates the modelled geometry with $\Delta z = 20d$ and $\alpha = 35^\circ$.

both locations the wall-normal height of the legs decreases as the structure passes, indicating the inclination as discussed above. At $x/\delta = 6$ the legs are further away from the wall, which is consistent with the vertical trajectory presented in Figure 3a. At this downstream position the vortices have spread compared to at $x/\delta = 3$, indicating a gradual breakdown of the vortical structure. The position of each vortex (z, y) is defined as the center of vorticity. These positions, combined with the relative streamwise position determined from the streamwise velocity as discussed above, lead to the three-dimensional structure of the legs presented in Figure 5. Apart from the offset in wall-normal position the two reconstructed structures (at $x/\delta = 3$ and 6) are similar. Both structures have a relatively constant inclination angle of $\alpha = 35^\circ$ and separation between their legs of $\Delta z = 20d$ as indicated by the black lines. With α and Δz assumed constant, the full geometry and strength of the vortical structures can be determined using planar-PIV (x, y) data only.

Calculation of induced velocity from planar-PIV

The vortex-induced velocity is determined from phase-locked velocity fields with the time-averaged incoming flow subtracted.

The process of calculating the vortex-induced velocity is described using Figure 6, corresponding to one of eight measured phases (results for the other seven phases are similar). The normalized relative streamwise (u^*/U_∞) and wall-normal (v^*/U_∞) velocity components are presented in (a) and (b) respectively. The relative components (u^* and v^*) are derived from the measured components (u and v) as

$$u^*(x, y) = u(x, y) - u_{in}(y), \quad (3)$$

with $u_{in}(y)$ the time-averaged incoming boundary-layer profile, averaged over $-1.7 < x/\delta < -1.0$ and

$$v^*(x, y) = v(x, y) - v_{in}(y) \approx v(x, y). \quad (4)$$

Selected vectors indicate the local (relative) velocity direction and magnitude. Close to the jet exit, there is a large wall-normal component, caused by the blowing of the jet. Further downstream, this wall-normal component becomes weaker, while the streamwise velocity deficit remains relatively constant, causing the shown velocity vector to tilt into the $-x$ -direction.

Arrow A indicates the calculation of the relative spanwise vorticity,

$$\omega_z^* = \frac{\partial v^*}{\partial x} - \frac{\partial u^*}{\partial y}. \quad (5)$$

The normalized vorticity, ω_z^*/ω_0 , is presented in Figure 6c. The relative spanwise vorticity indicates in-plane vortices moving with the flow as well as changes in shear compared to the shear in the incoming boundary layer. Two vortex pairs, originating from two cycles of the synthetic jet, are visible in Figure 6c. These vortex pairs form the head (blue, clockwise) and crossbar (red, counterclockwise) of the structure as presented in Figure 2.

In order to distinguish between (relative) vortices and shear layers present in the flow, the two-dimensional swirling strength method as described by Adrian *et al.* (2000) is used to identify vortices. The application of swirling strength to the relative vorticity field is indicated by arrow B. Figure 6d presents the normalized relative vorticity, ω_z^*/ω_0 , at locations identified as being a vortex only. Comparison of the full (relative) vorticity field (c) to the identified vortices (d) shows that indeed the vortices have been identified and (most of) the shear layers have been discarded. Note that unlike vorticity, swirling strength depends on non-linear operations. Therefore, following subtraction of the incoming flow, the identified vortices must be considered as purely relative vortices which do not necessarily have a vortical motion in the original velocity field. However, since the described analysis looks at the relative flow, the observed vortices are treated as actual vortices here.

Instead of analysing a single structure per vortex (as in Figure 2b), a hairpin filament (without crossbar) is modelled for each data-point identified as belonging to a vortex. The position of the hairpin filaments in relation to the vorticity field is presented in (e) where for clarity only one in ten filaments is shown. In practice, clockwise filaments (blue coloured, originating from the structures head) and counterclockwise filaments (red coloured, originating from the structures crossbar) partially merge in the hairpin legs, recreating the structure discussed above. This is equal to Figure 2a where the red and blue vortex filaments merge in the legs to form the red-blue dashed filaments.

Assuming potential flow, the velocity field induced by these vortex filaments can be calculated using Biot-Savart's law. In order

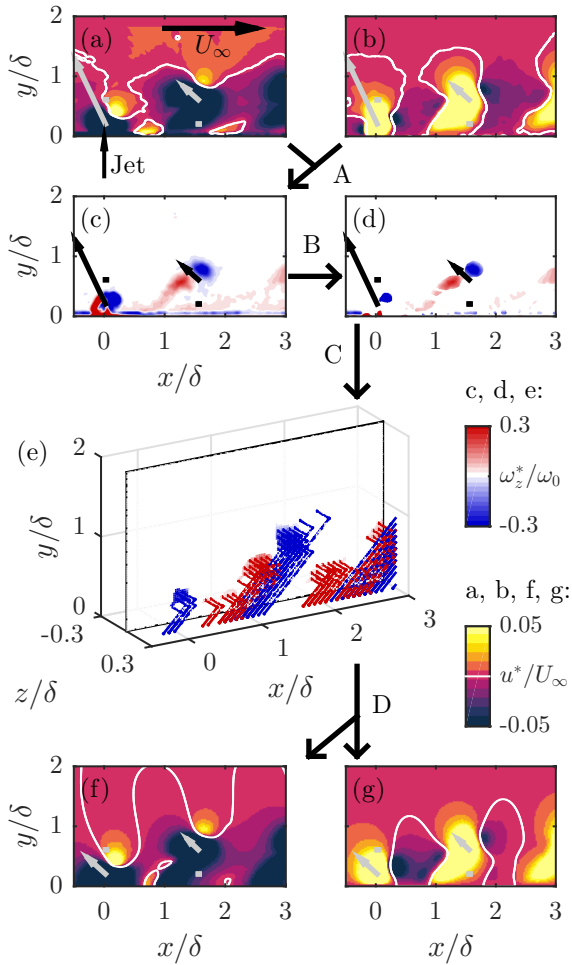


Figure 6. Phase-locked induced-velocity reconstruction process. Normalized relative streamwise- (a) and wall-normal (b) velocity components. Vorticity field calculated using these components (c) and vorticity of identified vortices only (d). Three-dimensional representation of hairpin vortices (e). For clarity only one in ten hairpins is displayed. Reconstructed streamwise- (f) and wall-normal (g) velocity components induced by vortices. Selected velocity vectors indicate local direction and magnitude.

to numerically apply Biot-Savart, each vortex filament is divided into small segments where the velocity induced by each segment is given by

$$\vec{u}_{ind,s}(x,y,z) = \frac{\Gamma}{4\pi} \frac{\vec{d}s \times \vec{r}}{|\vec{r}^3|}, \quad (6)$$

where $\vec{u}_{ind,s}$ is the velocity induced by the segment on a point (x,y,z) , $\vec{d}s$ is the vector containing the length of the segment in all three directions and \vec{r} is the position vector from the segment to the point. A convergence study showed that two segments per filament in the z -direction was sufficient to give reliable results. The same segment length ($\Delta z/2 = 10d$) is used in the legs of each filament. Since potential flow theory depends on linear equations, the contributions of all segments in all filaments can be added together to construct the full induced velocity field, i.e.

$$\vec{u}_{ind}(x,y,z) = \sum \vec{u}_{ind,s}(x,y,z). \quad (7)$$

The resulting streamwise and wall-normal induced velocity components are presented in (f) and (g) respectively. These induced velocity fields show similar features as the original velocity fields presented in (a) and (b).

Components that are discarded in this process include the effect of the jet blowing upwards, viscous blockage by the jet, the up wash effect and skin-friction effects. Features that are still visibly present include the streamwise velocity deficit inside each vortical structure, a streamwise acceleration above each structure and a significant positive wall-normal velocity component inside each structure. The remarkable qualitative similarity between the measured and induced velocity components indicates that the mentioned retained features are dominant over the discarded features.

The vortex-induced velocity as described above (and presented in Figure 6) for a single phase can be calculated for all eight phases to construct a time average. The measured time-averaged streamwise velocity component, relative to the incoming flow, is presented in Figure 7a. The white contour line indicates an equal velocity as in the incoming flow, i.e. above this line the velocity is slightly increased due to the presence jet. This is expected to be caused by the blockage of the jet – because of the conservation of mass, if part of the flow is blocked the velocity of the flow around it must increase. Figure 7b presents the induced time-averaged streamwise velocity component. This induced component is fully negative since the effect of blockage and mass-conservation is absent. Qualitatively the measured and induced velocity deficits are very similar. The difference between the two fields is presented in Figure 7c, where the contour-line from (a) is replotted. Three different regions can be identified. In region A the measured streamwise velocity is higher than the induced streamwise velocity (i.e. the measured velocity deficit is lower). This is the exact region where the measured velocity has increased compared to the incoming flow, indicating that the difference in this region is caused by the effect of blockage and mass-conservation discussed above. In region B the measured streamwise velocity is lower than the induced streamwise velocity. It is expected that this difference is caused by the effect of up wash, which is not present in the induced-velocity field. Up wash will transport low-momentum fluid from the surface upwards, decreasing the streamwise velocity. In region C the measured streamwise velocity is higher than the induced streamwise velocity. It is expected that this difference is caused by the same up-wash effect. The transport of low-momentum fluid from near the wall upwards will draw in high-momentum fluid towards the wall, increasing the streamwise velocity. The differences in regions B and C indicate a redistributing effect of streamwise momentum due to up wash.

The measured- and induced wake are compared quantitatively in terms of the momentum-flux deficit with respect to the incoming flow,

$$\Delta \dot{P}_x(x) = \int (\rho u_{in}^2 - \rho u^2) \hat{z} dy, \quad (8)$$

where ρ is the density and u is either the measured velocity or the velocity perturbed by the induced velocity ($u_{in} + u_{ind}$). This deficit in momentum flux is integrated over the wall-normal extent of the wake region (B and C in Figure 7c) and is per unit length in z -direction (\hat{z}).

This deficit in the momentum flux as function of streamwise position is presented in Figure 8 for both the measured and the induced wake. For both cases the momentum deficit sharply increases at the location of the jet (starting slightly upstream of the jet), reaches a maximum and becomes relatively stable after $x/\delta \approx 1$. The main reason for the sharp peak in the measured momentum-flux deficit is expected to be viscous blockage of the flow. Fluid

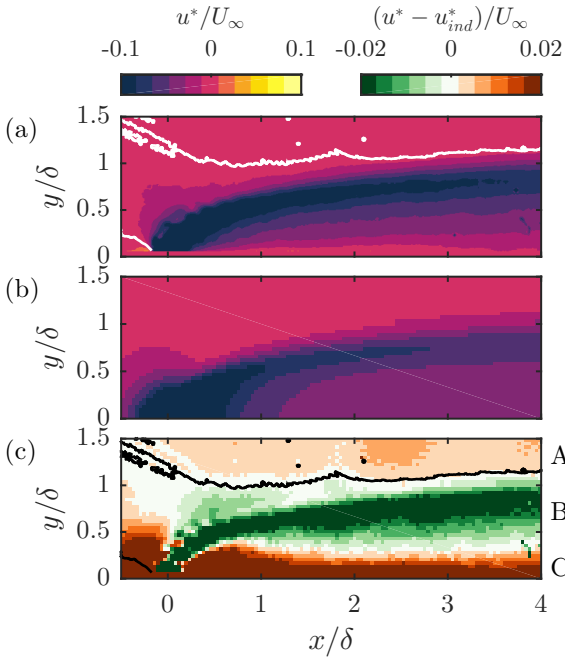


Figure 7. Time-averaged streamwise velocity deficit for measured (a) and induced (b) cases as well as the difference (c).

ejected by the synthetic jet has no streamwise velocity, causing momentum to be transferred from the cross flow to this fluid, thereby accelerating the fluid. It can be seen from the horizontal trajectory presented in Figure 3b that the vortices are quickly accelerated to a constant velocity, meaning that most of the blockage occurs close to the jet exit. Given the small spanwise extent of the jet, this blockage wake can be expected to recover quickly as indicated by the decrease in momentum deficit up to $x/\delta \approx 1$.

The peak in the induced momentum-flux deficit can not be caused by this viscous blockage, as this is not part of the potential flow model (which is inviscid). This peak is expected to be a start-up phenomenon related to the formation (roll up) of the vortical structures. This formation takes some time as can be seen in Figure 6. In the vorticity field in Fig. 6c, there is a vortex pair visible close to the jet exit ($x/\delta = 0$). However, the counterclockwise (red) vortex is not identified as a vortex by the swirling strength method and therefore discarded in Fig. 6d. In contrast, for the next vortex pair (around $x/\delta = 1.5$) the vortex is fully rolled up and properly identified.

The ratio between the measured and the induced momentum-flux deficits is presented in Figure 8b. This ratio is relatively constant downstream of $x/\delta = 1$, and averages around 0.9, meaning that 90% of the deficit in the measured momentum flux is accounted for by the induced velocity. This value is surprisingly high, given that in the literature the momentum deficit is mainly attributed to viscous blockage and up wash of low-momentum fluid. As discussed above, the effect of viscous blockage is expected to be recovered around $x/\delta = 1$, meaning that high-momentum fluid from the top and sides of the wake has filled in the momentum deficit caused by blockage. It should be noted that this does not actually recover the momentum deficit, it merely recovers it in our field of view (thereby decreasing the momentum outside our field of view).

Up wash by itself does not cause a momentum deficit, it merely redistributes regions of low- and high momentum. This is visible in Figure 7c where a region of decreased streamwise momentum (B) is visible above a region of increased streamwise momentum (C). This

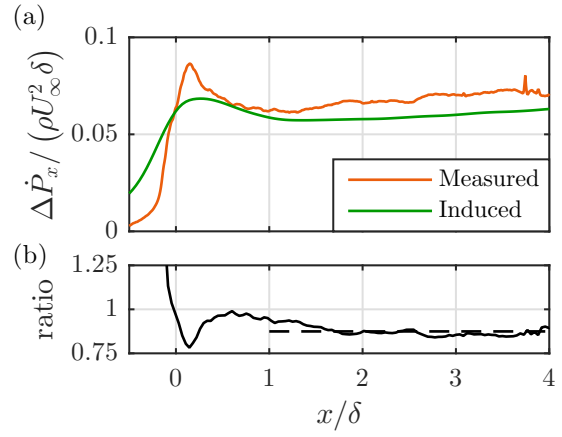


Figure 8. Measured and induced momentum deficit compared to the incoming flow as function of streamwise location (a). Ratio of the induced over the measured momentum deficit (b).

region of decreased momentum is created by the up wash of low-momentum fluid from near the wall. The up wash of this fluid draws in other (high-momentum) fluid from the sides, causing the region of increased momentum. As an effect of the increase in momentum near the wall the effect of skin friction will increase. The increase in skin friction may account for the 10% of momentum deficit not covered by the induced velocity.

FURTHER DISCUSSION

In the above analysis only the streamwise-wall-normal plane at $z/\delta = 0$ is considered. Figure 9 compares phase-locked velocity components relative to the incoming velocity measured using stereo-PIV in the plane at $x/\delta = 3$ to induced velocity components. The presented phase is equal to the phase presented in Figure 6. The left half of each graph shows the measured velocity while the right half shows the induced velocity. As in the analysis above, the same features are observed in the measured and induced velocity fields for all three components. As observed in the planar data, the streamwise velocity component (u^* , Fig. 9a) shows a velocity deficit between the legs of the hairpin. In contrast, outside of the hairpin there are small regions of an increase in streamwise velocity compared to the incoming flow. Likewise, the centerline of the plane showing the vertical velocity component (v^* , Fig. 9b) indicates a velocity directed away from the wall, while outside the hairpin the vertical velocity component is directed towards the wall. The spanwise velocity component (w^*) as presented in Figure 9c was not measured in the planar-PIV fields presented in this paper (and due to symmetry the spanwise velocity would be zero in the centerline plane). The spanwise velocity component shows a motion away from the centerline above the hairpin vortex and towards the centerline below the vortex. The fluctuations of velocity in all three planes is not surprising, given the circular nature of the velocity distribution around a vortex, but should be kept in mind when just considering the centerline as in the analysis of the present paper. The variation in Figure 9a indicates that the momentum deficit per unit length in z -direction measured at $z = 0$ (Fig. 8) should only be considered as such and not as a strength of the full (three-dimensional) wake.

In the analysis presented in this paper, a vortex filament is modelled at each data point recorded in the planar-PIV (as in Fig. 6e). An alternative model can be used by considering only a single filament per vortex (equivalent to the visualisation in Fig. 2b). The horizontal and vertical components of the velocity induced by this model are presented in Figure 10. Qualitative comparison to the induced velocity components in Figure 6f and g and the measured

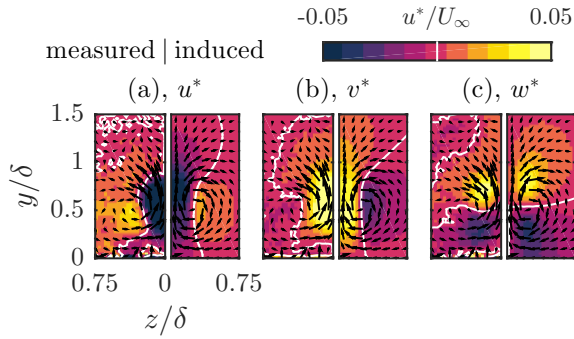


Figure 9. Comparison of phase-locked stereo-PIV data at $x/\delta = 3$ (left half of plots) to the computed induced velocity (right half) for the streamwise- (a), wall-normal (b) and spanwise (c) components.

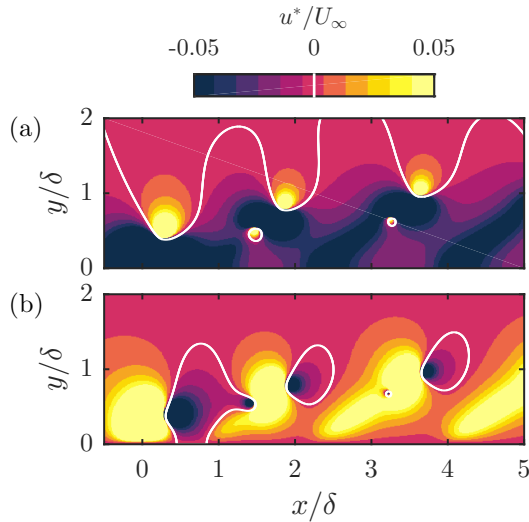


Figure 10. Streamwise (b) and wall-normal (c) components of the induced velocity calculated using the tracked vortices.

relative velocity in Figure 6a and b indicates that this model is less accurate than the the model used in the present paper. However, it might be possible to develop a predictive model based on tracked vortices. Vortex trajectories can be accurately described by power laws as presented in Figure 3. Together with the tracked vortex circulation as in Figure 11, all the parameters for the model can be described as function of time. It can be expected that the trajectories and (decay of) circulation can be expressed as function of Strouhal number and velocity ratio. This implies that a predictive model for the momentum deficit can be developed for different jet actuation parameters.

CONCLUSIONS AND OUTLOOK

The present paper has considered the momentum deficit created by a synthetic jet issuing in a turbulent boundary layer. It is shown that the three-dimensional geometry of vortex filaments created by the jet can be reconstructed using a combination of planar-PIV in the streamwise-wall-normal plane and stereo-PIV in the spanwise-wall-normal plane. This geometry shows a hairpin structure at an angle of $\alpha = 35^\circ$ and a spacing between the legs of $\Delta z = 20d$. Using these constant geometrical parameters, hairpin filaments can be modelled from the vorticity field measured in the planar-PIV plane. The velocity induced by these filaments is calculated by numerically applying Biot-Savart's law. Qualitatively, the

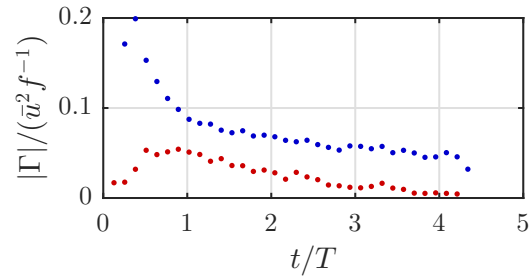


Figure 11. Tracked circulation for clockwise (blue) and counter-clockwise (red) spanwise vortices.

induced velocity components are very similar to the measured velocity components relative to the incoming flow. The streamwise-momentum-flux deficit per unit span at the centerline of the jet is calculated from both the measured and induced streamwise velocity. After some start-up behaviour up to $x/\delta \approx 1$ these momentum deficits are relatively constant. It is shown that nearly 90% of the measured momentum deficit can be ascribed to the induced velocity. The remaining 10% is expected to be caused by the down wash of high-momentum fluid towards the wall, increasing the momentum deficit due to skin friction. The potential of a model based on tracked vortices is presented qualitatively. This model seems to be less accurate than the model used in the present paper, but has the potential to be developed into a predictive model.

In future work the tracked vortex trajectories and circulation will be parametrized not only against time, but also against Strouhal number and blowing ratio of the jet. This will feed into a predictive model, indicating the induced momentum deficit without the need of experimental data for each case.

We acknowledge the financial support from the EPSRC (grant no. EP/L006383/1), ERC (grant agreement no. 277472) and the Royal Society International Exchanges Scheme.

REFERENCES

- Adrian, R. J., Christensen, K. T. & Liu, Z. C. 2000 Analysis and interpretation of instantaneous turbulent velocity fields. *Exps. Fluids* **29** (3), 275–290.
- Baidya, R., Philip, J., Hutchins, N., Monty, J. P. & Marusic, I. 2017 Distance-from-the-wall scaling of turbulent motions in wall-bounded flows. *Phys. Fluids* **29**, 020712.
- Dandois, J., Garnier, E. & Sagaut, P. 2007 Numerical simulation of active separation control by a synthetic jet. *J. Fluid Mech.* **574**, 25–58.
- Lardeau, S. & Leschziner, M. A. 2011 The interaction of round synthetic jets with a turbulent boundary layer separating from a rounded ramp. *J. Fluid Mech.* **683**, 172–211.
- M^cCloskey, R. T., King, J. M., Cortelezzi, L. & Karagozian, A. R. 2002 The actively controlled jet in crossflow. *J. Fluid Mech.* **452**, 325–335.
- Perry, A. E. & Chong, M. S. 1982 On the mechanism of wall turbulence. *J. Fluid Mech.* **119**, 173–217.
- Rathnasingham, R. & Breuer, K. S. 2003 Active control of turbulent boundary layers. *J. Fluid Mech.* **495**, 209–233.
- Sau, R. & Mahesh, K. 2008 Dynamics and mixing of vortex rings in crossflow. *J. Fluid Mech.* **604**, 389–409.
- de Silva, C. M., Hutchins, N. & Marusic, I. 2015 Uniform momentum zones in turbulent boundary layers. *J. Fluid Mech.* **786**, 309–331.